Tracer transport timescales and the observed Atlantic-Pacific lag in the timing of the Last Termination

Geoffrey Gebbie[1]

Received 27 December 2011; revised 15 May 2012; accepted 20 July 2012; published 6 September 2012.

[1] The midpoint of the Last Termination occurred 4,000 years earlier in the deep Atlantic than the deep Pacific according to a pair of benthic foraminiferal $\delta^{18}O$ records, seemingly implying an internal circulation shift because the lag is much longer than the deep radiocarbon age. Here a scenario where the lag is instead caused by regional surface boundary condition changes, delays due to oceanic transit timescales, and the interplay between temperature and seawater $\delta^{18}O$ ($\delta^{18}O_w$) is quantified with a tracer transport model of the modern-day ocean circulation. Using an inverse method with individual Green functions for 2,806 surface sources, a time history of surface temperature and $\delta^{18}O_w$ is reconstructed for the last 30,000 years that is consistent with the foraminiferal oxygen-isotope data, Mg/Ca-derived deep temperature, and glacial pore water records. Thus, in the case that the ocean circulation was relatively unchanged between glacial and modern times, the interbasin lag could be explained by the relatively late local glacial maximum around Antarctica where surface $\delta^{18}O_w$ continues to rise even after the North Atlantic $\delta^{18}O_w$ falls. The arrival of the signal of the Termination is delayed at the Pacific core site due to the destructive interference of the still-rising Antarctic signal and the falling North Atlantic signal. This scenario is only possible because the ocean is not a single conveyor belt where all waters at the Pacific core site previously passed the Atlantic core site, but instead the Pacific core site is bathed more prominently by waters with a direct Antarctic source.

Citation: Gebbie, G. (2012), Tracer transport timescales and the observed Atlantic-Pacific lag in the timing of the Last Termination, *Paleoceanography*, *27*, PA3225, doi:10.1029/2011PA002273.

1. Introduction

[2] A pair of $\delta^{18}O$ time series as recorded in benthic foraminifera shows that the midpoint of the Last Termination, as defined by the marine oxygen-isotope record [*Broecker and van Donk*, 1970], arrives about 4,000 years earlier in the Atlantic than the Pacific [*Skinner and Shackleton*, 2005]. A delay in the arrival of the deglacial $\delta^{18}O$ signal was anticipated due to the oceanic surface-to-deep transport time, estimated to be 1,000 to 3,000 years by *Mix and Ruddiman* [1984], and Pacific cores provided corroborating evidence for a delay of this duration [e.g., *Keigwin et al.*, 1992]. In a coarse resolution box model calibrated with modern-day radiocarbon observations, the isotopic signal of meltwater in the North Atlantic region was communicated to the deep Pacific in 1,750 years [*Broecker et al.*, 1988], while *Duplessy et al.* [1991] posited that the lag should be about 1,000 years as that is the deep Pacific radiocarbon age. The anticipated timescales are all shorter than the 4,000-year lag of *Skinner and Shackleton* [2005], however, suggesting that circulation changes or regional hydrographic differences are being detected in the Atlantic-Pacific pair of cores.

[3] One possibility is that the previous studies didn't resolve the processes that set radiocarbon with enough detail to accurately estimate the mean (or, equivalently, "ideal") age of ocean waters, defined as the average time elapsed since a parcel of water was last at the surface [e.g., *England*, 1995; *Hall and Haine*, 2002]. Estimation of age from radiocarbon requires detailed knowledge of the surface disequilibrium with the atmosphere (i.e., the reservoir age) [e.g., *Broecker and Peng*, 1982; *Matsumoto*, 2007], and any radio-age will differ from the ideal age in a way that depends upon the radioactive decay timescale and the mixing history along an ocean pathway [e.g., *Wunsch*, 2002; *Delhez et al.*, 2003]. Thus, radiocarbon ages that do not have a mixing correction are biased to be too young [e.g., *Deleersnijder et al.*, 2001]. Using a higher resolution box model and accounting for these biases, the deep Pacific age was revised a few hundred years upwards to nearly 1,500 years old [*Gebbie and Huybers*, 2012]. Even if this recent estimate is accepted, however, the observed paleoceanographic lag is still much longer.

[4] A further complication is that the ocean contains a whole range of tracer transport timescales, sometimes described as an age spectrum [e.g., *Delhez et al.*, 1999; *Hall*

[1]Department of Physical Oceanography, Woods Hole Oceanographic Institution, Woods Hole, Massachusetts, USA.

Corresponding author: G. Gebbie, Department of Physical Oceanography, Woods Hole Oceanographic Institution, MS 29, Woods Hole, MA 02543, USA. (ggebbie@whoi.edu)

0883-8305/12/2011PA002273

and Haine, 2002] or transit time distribution (TTD) [e.g., *Khatiwala et al.*, 2001; *Haine and Hall*, 2002], but it is not clear which timescales are most relevant to the Last Termination. The apparent lag between the ocean surface and interior does not equal the mean age [*Delhez and Deleersnijder*, 2008] and tracer timescales depend upon whether the injection of tracer is sudden or gradual [*Primeau and Deleersnijder*, 2009]. Timescales as long as 3,000 to 5,000 years can also be found, such as the time for equilibration to a surface shift [*Wunsch and Heimbach*, 2008]. If the surface injection is regional, rather than global, the timescale may be easily twice the mean age, as the time for water to cycle through the deep ocean before returning to the surface is comparable to the age itself [*Primeau and Holzer*, 2006]. There are multiple lags in the problem that can be defined, as well; here, we focus on the lag defined graphically in *Skinner and Shackleton* [2005, Figure 1]: the delay in the occurrence of the midpoint of the LGM-to-modern change.

[5] A few possible explanations for the 4,000 year lag include: (1) the relative chronology of the two cores being incorrect, (2) a more sluggish surface-to-deep circulation in the Pacific than the Atlantic, (3) the recording of distinct hydrographic changes through the temperature effect on calcification at the two core sites, (4) significant differences between the glacio-eustatic signal of δ^{18}O and the local δ^{18}O of seawater ($\delta^{18}O_w$), or (5) some combination of the above. Regarding (1), random uncertainties cannot create the lag without implying unrealistic climatic relationships in the North Atlantic such as extremely large reservoir ages [*Skinner and Shackleton*, 2005]. Should the chronology be modified in the future, we note that it is still inherently interesting to understand how such a lag could exist. For (2), radiocarbon evidence suggests that circulation rate changes are not large enough to explain the entire lag [e.g., *Shackleton et al.*, 1988; *Skinner and Shackleton*, 2004]. The investigation of (3) and (4) requires the simultaneous deconvolution of the two sediment core records into time-evolving temperature and $\delta^{18}O_w$ components, essentially an inversion of the global ocean circulation over thousands of years that is computationally prohibitive with general circulation models.

[6] The Total Matrix Intercomparison (TMI) method [*Gebbie and Huybers*, 2010, 2012] permits the computationally efficient decomposition of the modern-day ocean into when and where the water was last at the surface. Here, we turn this information into a model for the simulation of the transient transport of tracers that permits regional surface variability to occur, and the mixing coefficients that dominate the solution over long timescales are implicitly constrained by modern-day observations. Using this approach, we investigate (3) and (4) above by posing the question, is there any time evolution of sea surface temperature and $\delta^{18}O_w$ that can give rise to a 4,000 year interbasin lag? Thus, the experimental design is to model the transport of temperature and $\delta^{18}O_w$ over the last 35,000 years, to compare the δ^{18}O of calcite ($\delta^{18}O_c$) reproduced by the model with that observed in benthic foraminiferal records, and to adjust the surface boundary conditions in space and time to search for a consistent scenario. If the data is fit within its uncertainty, then the lag will also be captured and some combination of hypotheses (3) and (4) is capable of explaining what is seen in the Last Termination.

[7] While this work is designed to explore a range of solutions to the 4,000 year lag problem, some scenarios will not be explicitly modeled here, such as those where circulation pathways are subject to large shifts over time and those where surface tracer injections actively lead to circulation changes. Although recent modeling studies suggest that circulation pathways are fairly stable to meltwater injection because of boundary current trapping [*Condron and Winsor*, 2011], shifts in the water mass distribution and circulation pathways of the Last Glacial Maximum (LGM) have been interpreted in paleo-data [e.g., *Boyle and Keigwin*, 1982; *Curry and Oppo*, 2005; *Marchitto and Broecker*, 2006], and we suspect that a changed water mass distribution may be necessary to explain a more complete compilation of oxygen and carbon isotope data. For the purposes of understanding the 4,000 year lag, however, we will show that the interplay between temperature and $\delta^{18}O_w$ is sufficient to explain the data even without pathway variations.

2. Data

[8] The paleoceanographic data of interest is a pair of δ^{18}O records preserved in benthic foraminiferal calcite in sediment cores located at the Iberian margin (MD99-2334K, 38°N, 10°W, 3146 m depth) and the eastern equatorial Pacific (TR163-31B, 4°S, 84°W, 3210 m depth) [*Skinner and Shackleton*, 2005]. The chronology of Pacific core TR163-31B over the last 30,000 years is well constrained by 19 AMS ^{14}C dates performed on planktonic foraminifera [*Shackleton et al.*, 1988] and was originally calibrated based on the work of *Hughen et al.* [2004]. Here, we use a revised chronology (L. Skinner, personal communication, 2011) based on the Fairbanks0107 calibration [*Fairbanks et al.*, 2005] with tiepoints that are 1,000 years younger at 10 kyr BP (thousands of years before present) and up to 3,000 years younger at 20 kyr BP. The 1-σ errors are 100 to 600 years, increasing with age, although additional uncertainty is incurred by the constant reservoir age correction with the modern-day value of 580 years. Atlantic core MD99-2334K was originally placed on the Greenland ice core GISP2 age scale based on the similarity of planktonic δ^{18}O variations and corroboration with 10 planktonic foraminifer ^{14}C dates [*Skinner et al.*, 2003; *Skinner and Shackleton*, 2004]. Here core MD99-2334K is put on the SFCP04-GRIP timescale [*Shackleton et al.*, 2004] which makes negligible changes for times more recent than 20 kyr BP. For times older than 20 kyr BP, the SFCP04-GRIP timescale is 500 to 1,000 years older than the original published chronology. The Atlantic-Pacific lag in the midpoint of the Termination is increased by about 250 years with the revised chronology.

3. Model

3.1. Green Functions for Tracer Transport

[9] The goal of the model is to reconstruct $\delta^{18}O_c$ at the two core sites in a way that follows a reasonable set of circulation pathways and rates. As $\delta^{18}O_c$ in foraminifera depends on both the ambient $\delta^{18}O_w$ and temperature, both tracers are modeled. If geothermal heating is small, both $\delta^{18}O_w$ and potential temperature, θ, are conservative tracers away from the sea surface that follow an advective-diffusive

equation that can be efficiently formulated in terms of Green functions (also see their application in mathematical physics [e.g., *Morse and Feshbach*, 1953], seismology [e.g., *Hartzell*, 1978], and many other fields). In particular, the interior concentration of any conservative tracer at a given point and time, $C(r, t)$, is a combination of contributions from source waters that were at the surface at previous times (see Appendix A):

$$C(r,t) = \sum_{i=0}^{N_t-1} \left[\mathbf{g}(i)^T \, \vec{C}_{sfc}(t - i\Delta t) \right], \tag{1}$$

where $\mathbf{g}(i)$ is a vector that represents the surface pattern of fractional contributions that arrive with a lag of i timesteps, the vector transpose is denoted ^{T}, and $\vec{C}_{sfc}(t - i\Delta t)$ is the vector containing the surface concentration of the tracer (θ or $\delta^{18}O_w$) at time $t - i\Delta t$. Time is discretized with a timestep, Δt, of 500 years for the time interval from 40 kyr BP to the present-day. The summation is valid when N_t is large enough to account for all of the previous timesteps that affect the tracer concentration (with no contribution from future times); here we confirm that 10,000 years is long enough to capture more than 99.9% of the ocean's memory at the core sites, corresponding to $N_t = 20$ timesteps. Besides time discretization, the surface sources are discretized onto a grid with $4^\circ \times 4^\circ$ horizontal resolution, leading to $N_{xy} = 2806$ surface boxes, and thus each vector $\mathbf{g}(i)$ has 2,806 elements. Equation (1) can also be expressed as a double summation over time and the space of the entire surface.

[10] The collection of $\mathbf{g}(i)$ functions at all times has been termed the multiple-source boundary propagator [*Haine and Hall*, 2002] or the boundary Green function [*Wunsch*, 2002], and *Gebbie and Huybers* [2012] demonstrate that it can be determined from modern-day tracer observations. The boundary Green function could be calculated by perturbing the surface tracer concentration at previous times and locations, but there are 2,806 surface boxes that would each need an integration of the advection–diffusion equations over many thousands of years. Instead the adjoint of the tracer transport equation is used to compute $\mathbf{g}(i)$, which requires just one integration for each core site (see Appendix A and *Primeau* [2005]). In order to accurately resolve tracer transport, $\mathbf{g}(i)$ is computed offline with 33 vertical levels and a timestep that is much shorter than the time resolution of the surface boundary conditions. Then, the high resolution $\mathbf{g}(i)$ is linearly interpolated onto the proper surface times for use in the tracer inversion. These Green functions encapsulate the essential elements of the modern-day global circulation as diagnosed from a modern-day suite of tracer observations from the World Ocean Circulation Experiment (WOCE) climatologies [*Gouretski and Koltermann*, 2004], the GISS $\delta^{18}O_w$ data set [*LeGrande and Schmidt*, 2006], and the Global Ocean Data Analysis Project (GLODAP) natural radiocarbon data set [*Key et al.*, 2004].

3.2. Paleotemperature Equation

[11] To translate potential temperature to the needed in-situ temperature, we use a nonlinear equation for the compressibility effect [*Fofonoff and Millard*, 1983]: $T = \mathcal{T}(\theta, S, p)$, where S is set to a mean salinity of 35 and pressure, p, is set according to the core depth of interest. Furthermore, we use a nonlinear paleotemperature equation [*O'Neil et al.*, 1969; *Shackleton*, 1974] with a 0.27‰ offset between VSMOW and VPDB standards: $T = 16.9 - 4.38(\delta^{18}O_c - \delta^{18}O_w) + 0.1(\delta^{18}O_c - \delta^{18}O_w)^2$. Solving this quadratic equation for $\delta^{18}O_c$, we symbolically write, $\delta^{18}O_c = f(\delta^{18}O_w, T)$. Substituting equation (1) and the in-situ temperature equation here, we obtain one nonlinear equation for the sediment core values given surface tracer conditions:

$$\delta^{18}O_c(t) = f\left\{ \sum_{i=0}^{N_t-1} \left[\mathbf{g}(i)^T \vec{\delta}^{18}O_w^{sfc}(t - i\Delta t) \right], \mathcal{T}\left\{ \sum_{i=0}^{N_t-1} \left[\mathbf{g}(i)^T \vec{\theta}_{sfc}(t - i\Delta t) \right] \right\} \right\}, \tag{2}$$

where $\vec{\delta}^{18}O_w^{sfc}(t)$ and $\vec{\theta}_{sfc}(t)$ are the surface source vectors at time t. The formulation of equation (2) is advantageous because the global tracer distribution need not be calculated, only tracer concentrations at the core locations.

4. Inverse Method

[12] Given the modern-day circulation pathways and a past estimate of surface $\delta^{18}O_w$ and θ, we have a means of estimating $\delta^{18}O_c$ at the core locations. Appending the surface source vectors for all times, $\vec{\delta}^{18}O_w^{sfc}(t)$ and $\vec{\theta}_{sfc}(t)$, into one vector of unknowns, $\mathbf{x}$, we search for a solution to the set of simultaneous equations,

$$\mathcal{G}[\mathbf{x}] = \vec{\delta}^{18}O_c^{obs} + \mathbf{n}, \tag{3}$$

where $\mathcal{G}$ is a nonlinear operator composed of equations of the form of (2) where the proper $\mathbf{g}(i)$ functions are placed on the right chronology and the right core location, each row of $\mathcal{G}$ corresponds to an observational constraint, $\vec{\delta}^{18}O_c^{obs}$ is the vector of $\delta^{18}O_c$ observations, and $\mathbf{n}$ is the observational error. The problem addressed in this work is to search for a time-evolving pattern of the surface $\delta^{18}O_w$ and θ (i.e., $\mathbf{x}$) that satisfies (3), to infer whether the interplay of these two tracers can explain the observed lag.

[13] With a good first guess, $\mathbf{x}_0$, all solutions can be written in the form, $\mathbf{x} = \mathbf{x}_0 + \mathbf{u}$, and equation (3) is linearized to simplify the solution method:

$$\mathbf{G}\mathbf{u} = \mathbf{y} + \mathbf{n}, \tag{4}$$

where $\mathbf{G} = \partial\mathcal{G}/\partial\mathbf{x}]_{\mathbf{x}_0}$ and $\mathbf{y} = \delta^{18}O_c^{obs} - \mathcal{G}[\mathbf{x}_0]$. To determine whether a solution is acceptable, a cost function is defined as the sum of squared data-model misfits: $J_{data} = (\mathbf{G}\mathbf{u} - \mathbf{y})^T\mathbf{W}^{-1}(\mathbf{G}\mathbf{u} - \mathbf{y})$, where $\mathbf{W}^{-1}$ is a diagonal matrix with $1/\sigma^2$ on the diagonal and $\sigma = 0.08$‰ is the analytical precision of the stable isotopes [*Shackleton et al.*, 1988; *Skinner et al.*, 2003]. If the data-model misfit is within the expected uncertainty, then J_{data} will be approximately equal to N_{obs}, the number of observations. We find that the linearization is successful due to the paleotemperature equation being only weakly nonlinear and that the solution also holds for the fully nonlinear model (2).

[14] We implement a first guess solution, $\mathbf{x}_0$, that agrees with modern-day $\delta^{18}O_w$ [*LeGrande and Schmidt*, 2006] and temperature data [*Gouretski and Koltermann*, 2004], the magnitude of changes over the Last Termination informed by *Adkins et al.* [2002], and the timing of the Last Glacial Maximum. In particular, we start with the overly simple notion that variations at the sea surface were globally uniform and linear in three segments: before 18 kyr BP, between 18 and 9 kyr BP, and after 9 kyr BP. At each surface location, the baseline linear trend is set by the first-guess LGM-to-modern difference, the glacial period is guessed to have trends that are 15% as large as the Termination in the opposite sign, and the Holocene has no trend. To satisfy these constraints, a term is added to the cost function: $J_{xy} = \mathbf{u}^T\mathbf{S}_{xy}^{-1}\mathbf{u}$, where $\mathbf{S}_{xy}^{-1}$ is a nondiagonal matrix that enforces spatial variability to be smooth on a length scale of 1,000 km as those are the spatial scales that are expected to be preserved in paleo-data, and this also serves as a numerical device to suppress gridscale noise in the solution [*Bennett*, 1992; *Gebbie et al.*, 2006]. The J_{xy} term also enforces a constraint on the magnitude of differences from the first guess, where we assume that the modern-day boundary conditions are known within 0.07‰ and 0.28°C, consistent with the instrumental record, and past values are only weakly known within uncertainty of 1‰ and 4°C.

[15] As the solution, $\mathbf{x}$, contains concentrations from all times, we have a "whole domain" formulation that also allows temporal smoothing constraints. Here we put a constraint on the size of temporal variability with a cost function term

$$J_t = \alpha_t^2 \sum_{i=1}^{N_t} \sum_{j=1}^{14} \left\{ \mathbf{r}_j^T \left[\vec{C}_{sfc}(-i\Delta t) - \vec{C}_{sfc}(-i\Delta t + \Delta t) \right] \right\}^2, \quad (5)$$

where $\mathbf{r}_j$ is a vector that averages the source values into 14 water mass sub-regions such as the Labrador, Nordic, Weddell, and Ross Seas (for a complete list, see *Gebbie and Huybers* [2011, Figure 7]), and J_t is evaluated for both $\delta^{18}O_w$ and θ (in place of the symbolic $\vec{C}_{sfc}$ above). Here, we expect the time change of the average source values to vary by 0.2‰ or 0.8°C per timestep of 500 years, and thus α_t = 1/(0.2‰) or 1/(0.8°C). This parameter is based upon the characteristics of the data, where scatter as large as 0.3‰ is seen in data points separated by just a few hundred years, and we do not believe that all of the scatter should be fit exactly. Furthermore, the focus of this work is on the longer timescale of the general trend of the Last Termination. In matrix form, the additional cost function term is $J_t = \mathbf{u}^T\mathbf{F}^T\mathbf{W}_t\mathbf{F}\mathbf{u} \equiv \mathbf{u}^T\mathbf{S}_t^{-1}\mathbf{u}$, where $\mathbf{F}$ performs the water mass averaging and differencing in (5), the tracer values in (5) are anomalies referenced to the first guess, and $\mathbf{W}_t$ is a weighting matrix with α_t^2 on the diagonal.

[16] The complete cost function is combined from the foregoing 3 parts, $J = J_{data} + J_{xy} + J_t$:

$$J = (\mathbf{G}\mathbf{u} - \mathbf{y})^T\mathbf{W}^{-1}(\mathbf{G}\mathbf{u} - \mathbf{y}) + \mathbf{u}^T\left(\mathbf{S}_{xy}^{-1} + \mathbf{S}_t^{-1}\right)\mathbf{u}, \quad (6)$$

where the two covariance matrices $\mathbf{S}_{xy}$ and $\mathbf{S}_t$ could be written as one, but there are 451,766 unknowns to be estimated, and the special structure of the equation with the two covariance matrices is exploited to render the problem computationally tractable (see Appendix B for the complete solution).

5. Results

5.1. Temporal Evolution at the Core Sites

[17] We find time-evolving surface boundary conditions with regional variations that fit the Atlantic and Pacific $\delta^{18}O_c$ data within their stated errors (Figure 1). The normalized cost function value, J_{data}/N_{obs}, is 1.15, indicating a standard error of 0.12‰ and consistency within the expected error level. More specifically, the Atlantic is fit with a standard error of 0.11‰ and the Pacific 0.13‰, where the lag between the two is captured. We find that the maximum lagged cross-correlation between the two time series is at 3,825 years, near the 3,900 years found by *Skinner and Shackleton* [2005], but, more importantly, the fit is obtained without any internal change in the circulation pathways or rates. The lag in the observations is explained here by shifts in the $\delta^{18}O_w$ and θ end-members and the consequent ocean transit times to the core locations.

[18] The inverse solution suggests that the 1.8‰ LGM-to-modern $\delta^{18}O_c$ change at the Iberian margin core is contributed nearly equally by temperature and $\delta^{18}O_w$ changes (Figure 2). The estimated temperature is as cold as −0.8°C during glacial times, rising to a well-reproduced modern-day temperature of 2.8°C, yielding a 0.98‰ effect on $\delta^{18}O_c$ (using − 0.27‰/°C consistent with the paleotemperature equation). The misfit between the estimated temperature and Mg/Ca data [*Skinner et al.*, 2003] has a standard deviation of 0.8°C, near the estimated Mg/Ca-derived temperature uncertainty of 0.7°C. Before 18 kyr BP, however, the estimated temperature is on average 0.4°C warmer than the Mg/Ca data suggests, and such a mean misfit would represent an inadequacy of the model if the data calibration were known exactly. In light of remaining uncertainties in the interpretation of Mg/Ca, however, such a misfit is probably still within the expected error bounds.

[19] The full range of $\delta^{18}O_w$ at the Iberian margin is estimated to be 1.01‰, giving a roughly equal effect on $\delta^{18}O_c$ as temperature. Due to an increase in $\delta^{18}O_w$ in the last 4,000 years, however, the LGM-to-modern change is smaller at 0.8‰. The character of this 4,000 year interval is dependent upon matching the modern-day boundary conditions, which in turn is dependent upon the paleotemperature equation used. If the equation of *Erez and Luz* [1983] is used instead, there is no rise in $\delta^{18}O_w$ over this time, with direct impact on the inferred glacial-modern difference.

[20] Following the same Green function technique used at the core sites, the global mean $\delta^{18}O_w$ is also reconstructed, and we find a LGM-modern difference of 1.04‰, reflecting the glacioeustatic change due to melt of land ice. The glacioeustatic effect is slightly larger than the 1.0‰ inferred from pore water samples [*Adkins et al.*, 2002], a difference that will be addressed later. The difference between the local and global mean $\delta^{18}O_w$ is as large as 0.8‰ at the Iberian margin 12 kyr BP, showing the large impact of regional effects.

[21] The inverse model shows coupling between temperature and $\delta^{18}O_w$ along the Iberian margin, although much of coupling occurs at millennial scales that are shorter than the

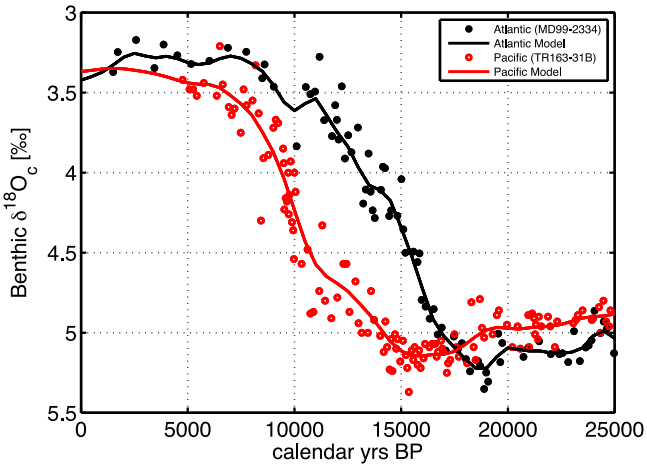

Figure 1. Benthic foraminiferal $\delta^{18}O_c$ (‰ VPDB) recorded in Iberian margin core MD99-2334K (black dots) and reconstructed by the inverse model (black line), as well as $\delta^{18}O_c$ recorded in eastern Pacific core TR163-31B (red dots) and reconstructed by the inverse model (red line).

timescales of focus here. The movement of water mass boundaries has been thought to play a role in this coupling, but in this model, the sources of waters are fixed through time and the coupling is accomplished through changes in end-member values. Information from carbon isotope records may permit these two scenarios to be distinguished.

[22] At the eastern Pacific core site TR163-31B, the inversion estimates an LGM-modern difference of 1.2‰ in $\delta^{18}O_w$ and 2.4°C in temperature, with the $\delta^{18}O_w$ influence on $\delta^{18}O_c$ about twice as large as temperature (Figure 3). Mg/Ca data from *Uvigerina* sp. indicate a temperature difference less than 2°C [*Martin et al.*, 2002], but Mg/Ca data from *G. affinis* indicate that the deep Pacific may have been close to the freezing point [*Skinner and Shackleton*, 2005]. Due to the remaining uncertainty, the Mg/Ca data have not been plotted, and we note that the inverse solution is somewhere between the two Mg/Ca interpretations. For $\delta^{18}O_w$, the inverse solution shows that a nonglacioeustatic signal of 0.2‰ is possible even in the Pacific. While the Pacific core $\delta^{18}O_w$ follows the global mean $\delta^{18}O_w$ more closely than the Atlantic core, significant deviations exist and the timing of variations differ by 2,000 years around 17 kyr BP.

[23] To determine whether the glacial-interglacial changes are reasonable, the reconstructed surface fields are used to estimate the time evolution of $\delta^{18}O_w$ and $\delta^{18}O_c$ at the four locations of pore water data in *Adkins et al.* [2002]. Even without an explicit pore water constraint, the inverse solution predicts a smaller $\delta^{18}O_w$ difference in the North Atlantic cores relative to the Southern Ocean cores (Table 1). The model solution fits three of the four $\delta^{18}O_w$ values within their published errors, and three of the four $\delta^{18}O_c$ values within 0.2‰, a reasonable error level. While the predicted Chatham Rise $\delta^{18}O_w$ shift is outside the published 2σ error bound, statistical tests indicate that the model misfits of the combined 8 pore water $\delta^{18}O_w$ and $\delta^{18}O_c$ data are not large enough to convincingly claim that the circulation pathways changed in the past (at the 5% insignificance level, z-test: $p = 0.06$, chi-squared test: $p = 0.15$), and the reported 2σ errors may not account for other systematic errors. Furthermore, the pore water data have not been explicitly used to constrain the model and a better fit is likely possible. While the combination of pore water and other calcite constraints is a promising way to look for circulation shifts in the past, this study finds that the modern-day circulation does an adequate job of describing what is seen at 6 core locations of interest here.

5.2. Spatial Patterns of Variability

[24] The spatial pattern of surface $\delta^{18}O_w$ throughout the last 25,000 years is reminiscent of the modern-day pattern (Figure 4). In part this is by construction, as the data do not

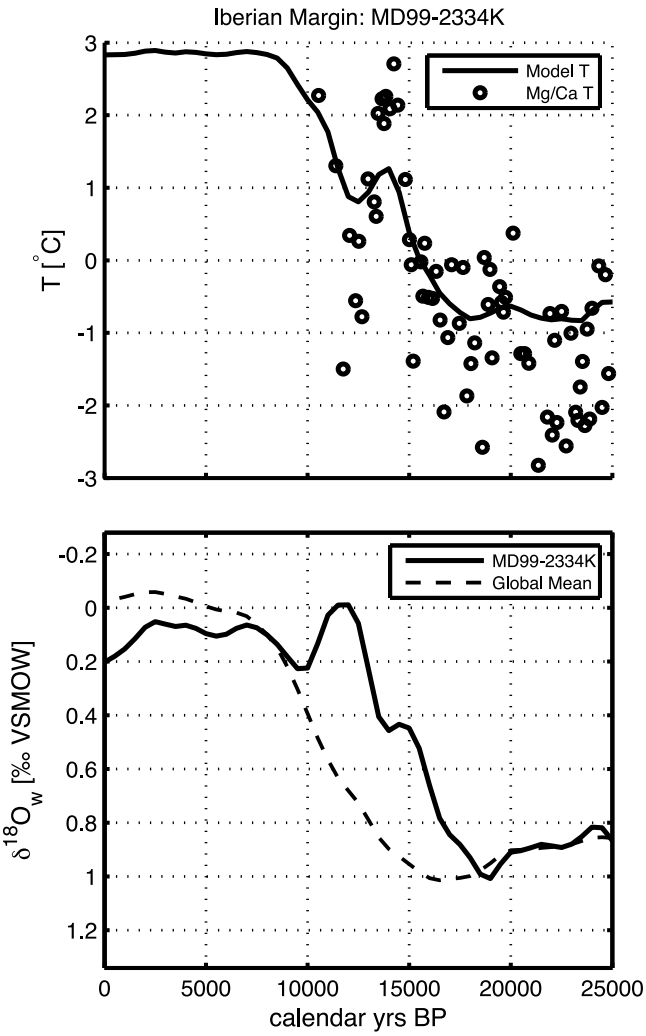

Figure 2. Temperature-$\delta^{18}O_w$ time evolution at the Iberian margin MD99-2334K core site. (top) Reconstructed deep water temperature (black line) versus Mg/Ca-derived temperatures [*Skinner et al.*, 2007] (black circles). (bottom) Reconstructed local $\delta^{18}O_w$ (black line) versus the reconstructed global mean $\delta^{18}O_w$ (dashed line). The two panels are scaled so that vertical changes correspond to a similar effect on $\delta^{18}O_c$.

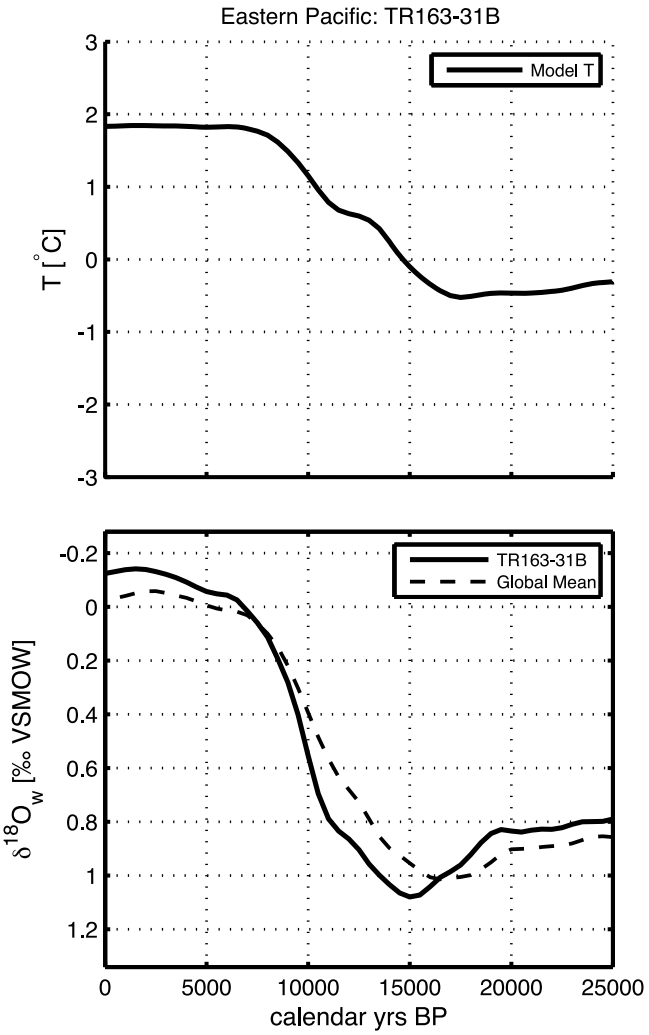

Figure 3. Temperature-$\delta^{18}O_w$ time evolution at the eastern Pacific TR163-31B core site. (top) Reconstructed deep water temperature (black line). (bottom) Reconstructed local $\delta^{18}O_w$ (black line) versus the reconstructed global mean $\delta^{18}O_w$ (dashed line).

require large deviations from the first guess based upon the modern-day pattern. That this pattern is relatively unaltered and the data could still be fit, however, was not obvious a priori, as it implies that no major changes in the pattern of evaporation or precipitation are necessary. Regional changes to $\delta^{18}O_w$ certainly exist, such as in the Weddell and Ross Seas where local $\delta^{18}O_w$ is reconstructed to be higher than the neighboring areas, and the modern-day distribution reflects a remnant of this signal. Overall, though, regional changes are not immediately apparent because the tracer's spatial range at any given time is considerably larger than the LGM-to-modern difference. Thus, slight shifts in the geographic location of the background field may have large effects on local conditions.

[25] The regional changes that are necessary to fit the data are emphasized in maps of $\delta^{18}O_w$ anomalies defined relative to modern-day values (Figure 5). At 21 kyr BP, the Nordic Seas have the lowest $\delta^{18}O_w$ waters while both the Weddell and Ross Seas have waters with high $\delta^{18}O_w$ values relative to the global mean. All the way through 7 kyr BP, the North Atlantic surface leads the global change and the Antarctic region lags with $\Delta(\delta^{18}O_w)$ variations peaking above 1‰ at 7 kyr BP in the Southern Ocean. The modern-day reconstruction closely fits the GISS data set [*LeGrande and Schmidt*, 2006]. As anticipated, the modeled evolution of $\delta^{18}O_w$ is more complex than the global glacioeustatic signal.

[26] The LGM-to-modern difference in surface temperature is small relative to spatial differences at any given time, especially due to the large gradients at the polar fronts (Figure 6). As expected, the area of the sea surface below 0°C was expanded in the Southern Ocean at 21 kyr BP, and the North Atlantic polar front moves northward over the Last Termination. While anomaly maps showed north–south shifts in the surface pattern of $\delta^{18}O_w$ over time, the surface temperature anomaly has a consistent spatial pattern with a decreasing amplitude over time (Figure 7). The freezing point of water puts a large constraint on this spatial pattern, which is enforced in the inverse method by putting tight constraints on waters that are already near the freezing point in the first-guess solution (via the cost function term, J_{xy}). Thus, the polar regions do not have a large glacial-interglacial signal in temperature because they are already near the freezing point in the modern-day. The major signal is instead seen in the subpolar and subtropical North Atlantic where a 6°C change is inferred from the core data.

[27] Relative changes are analyzed by averaging the surface values in the southern versus northern source regions, where the southern source is defined as all southern hemisphere water originating from the surface south of the subtropical front (see ANT and SUBANT regions in *Gebbie and Huybers* [2010]), and the northern source includes all

Table 1. Circulation Properties at the Location of the Benthic Foraminiferal Cores, Pore Water Data Locations, and the Global Ocean[a]

Location	Name	m_S	m_N	$\bar{a}$ (years)	$\Delta(T)(^\circ C)$	$\Delta(\delta^{18}O_w)$(‰)	$\Delta(\delta^{18}O_c)$(‰)
Iberian Margin	MD99-2334K	13	81	419	3.66	0.81	1.80
Eastern Pacific	TR163-31B	74	23	1264	2.35	1.20	1.78
Bermuda Rise	ODP 1063	12	84	438	3.28	0.79	1.68
Feni Drift	ODP 981	6	88	118	4.20	0.79	1.92
Chatham Rise	ODP 1123	80	18	719	2.04	1.28	1.77
Shona Rise	ODP 1093	65	33	596	1.85	1.28	1.76
Global Ocean		56	31	715	2.71	1.04	1.77

[a]Benthic foraminiferal cores from *Skinner and Shackleton* [2005]; pore water data locations from *Adkins et al.* [2002]. The columns refer to the percentage of water originating from a southern source (m_S) or a northern source (m_N) where the exact surface source regions are defined later, the mean age of waters ($\bar{a}$), and the absolute value of the LGM-modern difference in temperature, $\delta^{18}O_w$, and $\delta^{18}O_c$ ($\Delta(T)$, $\Delta(\delta^{18}O_w)$, and $\Delta(\delta^{18}O_c)$). The entries are presented with more significant digits than warranted by their remaining uncertainty in order to detail this scenario.

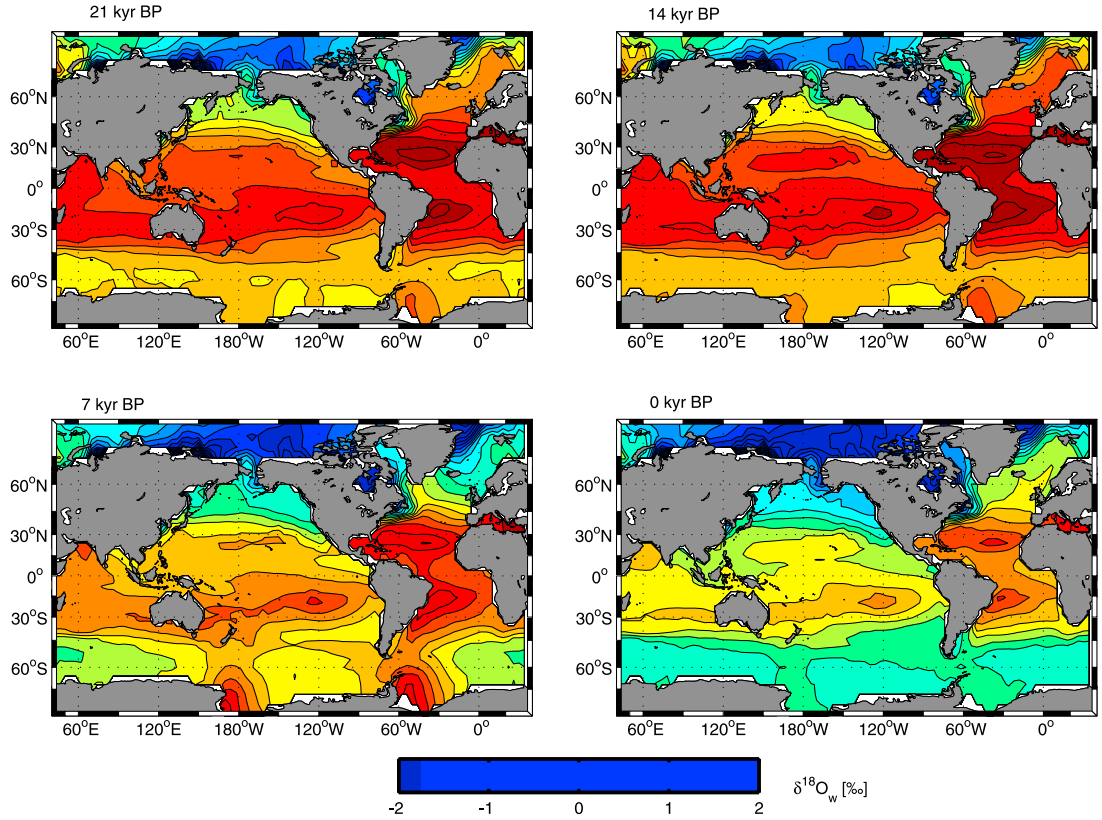

Figure 4. Surface concentration of $\delta^{18}O_w$ at 21 kyr BP, 14 kyr BP, 7 kyr BP, and 0 kyr BP (contour interval: 0.25‰).

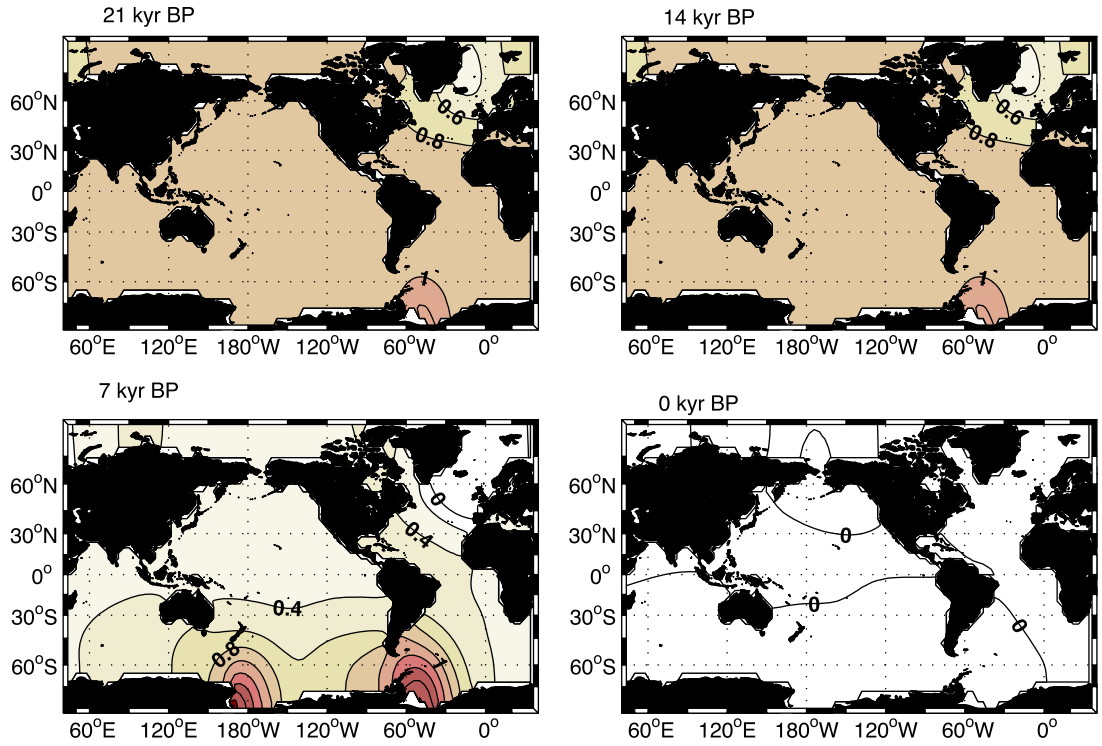

Figure 5. Surface concentration of $\Delta(\delta^{18}O_w)$ at 21 kyr BP, 14 kyr BP, 7 kyr BP, and 0 kyr BP, defined as the difference to the modern-day GISS $\delta^{18}O_w$ data set of *LeGrande and Schmidt* [2006] (contour interval: 0.2‰).

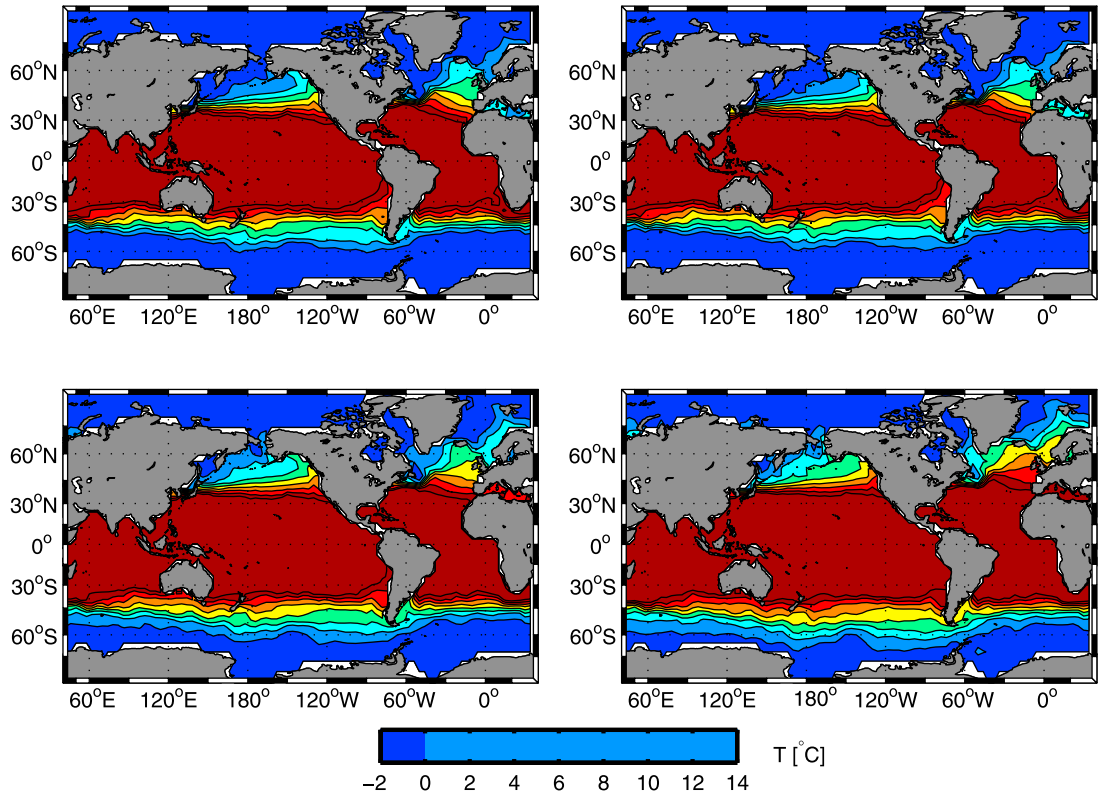

Figure 6. Same as Figure 4, but with surface temperature at 21 kyr BP, 14 kyr BP, 7 kyr BP, and 0 kyr BP (contour interval: 2°C).

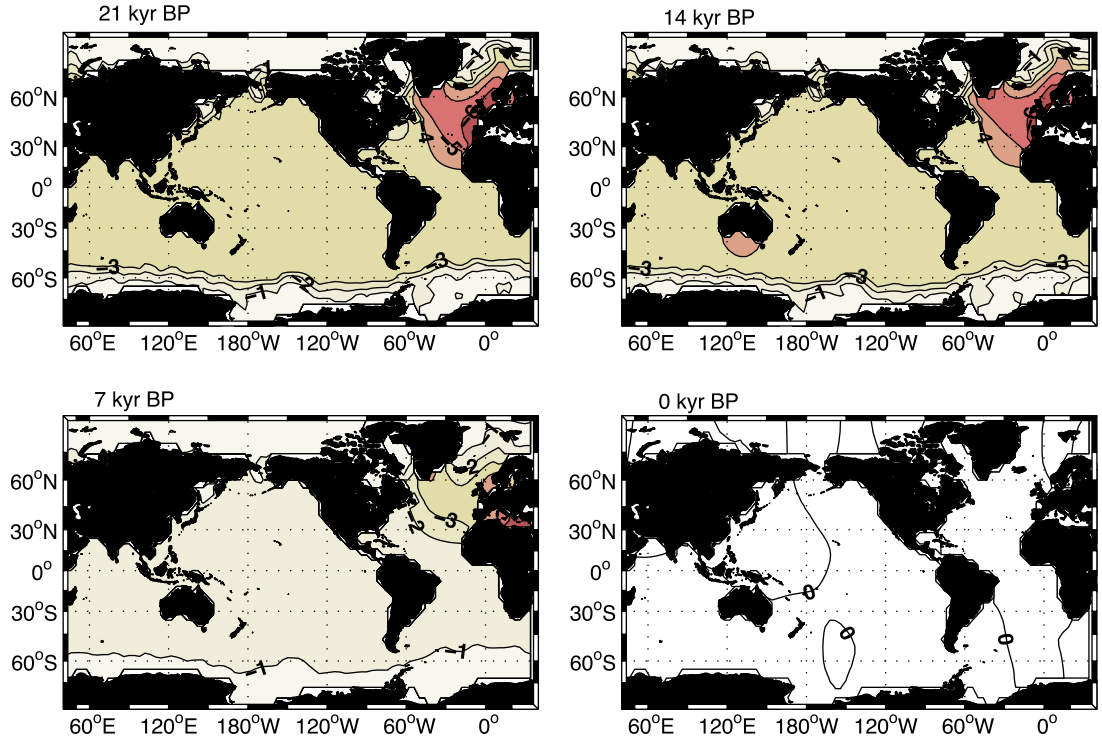

Figure 7. Same as Figure 5, but with $\Delta(T)$, the surface temperature anomaly defined relative to the modern day value of *Gouretski and Koltermann* [2004], at 21 kyr BP, 14 kyr BP, 7 kyr BP, and 0 kyr BP (contour interval: 1°C).

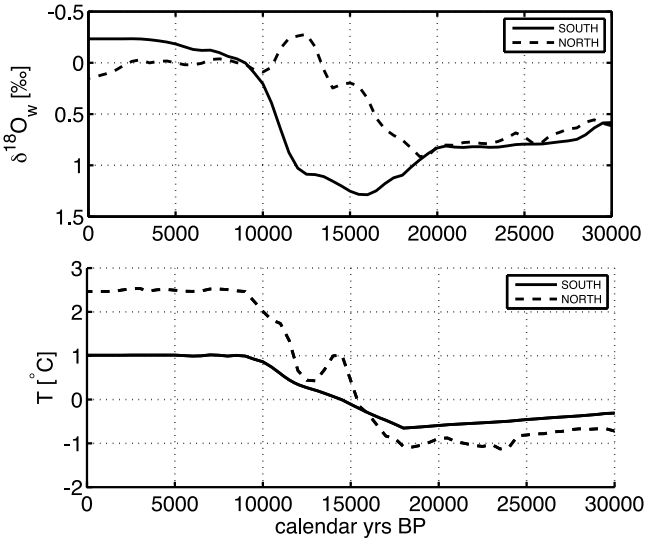

Figure 8. Time series of northern- and southern-source end-member values, for (top) $\delta^{18}O_w$ and (bottom) temperature. The definition of the source waters is given in the text.

water originating from the subpolar and Arctic regions of the northern hemisphere (i.e., NATL, NPAC, and ARC regions). In accordance with the spatial map, the source waters have widely differing $\delta^{18}O_w$ values (Figure 8). While the spatial map appeared to show opposing changes in the North Atlantic and Antarctica, the time series of average surface properties shows that the peak $\delta^{18}O_w$ occurs later in the Antarctic region, giving opposing trends between the two hemispheres from 19 to 16 kyr BP. Relative sea level data shows that the local Last Glacial Maximum was delayed in the Western Antarctic Ice Sheet and the Southern Hemisphere [*Clark et al.*, 2009], providing support for the inferred late southern $\delta^{18}O_w$ maximum seen here. Thus, we suggest that the continued increase of the southern surface $\delta^{18}O_w$ up to 16 kyr BP is explained by the continuation of the glacial trend, and that the southern hemisphere freshwater cycle remained in a glacial state for a few thousand years longer than the northern hemisphere.

6. Discussion

6.1. Tracer Transport Interference

[28] The previous section detailed the interplay between $\delta^{18}O_w$ and temperature, but it did not explain how a lag that is longer than the age of ocean waters may appear. Consider an idealized case where two sediment cores record the signal of the Last Termination in tracer c with the form of a hyperbolic tangent function:

$$c(t) = a\left[\tanh\frac{(t - t_{mid})\pi}{T_D}\right] + c_{mid}, \qquad (7)$$

but the midpoint of the Termination, t_{mid}, is 4,000 years earlier in one core versus the other. Furthermore, suppose that the sediment cores are bathed in waters from just two sources, the interior pathways are unchanging, and surface-to-deep transit times are negligibly small. Labeling the cores "A" and "B", conservation of tracer gives: $m_{A1}c_1(t) + m_{A2}c_2(t) = c_A(t)$, and $m_{B1}c_1(t) + m_{B2}c_2(t) = c_B(t)$, where m_{A1} is the fraction of water at core "A" that originates from source 1, and the other m variables are defined accordingly. At time t, one can solve for source values, c_1 and c_2, by inverting the set of two simultaneous equations.

[29] Using information from the boundary Green function (equation (1)), we can set the m values in the idealized example to roughly correspond to northern and southern source contributions. The sum of the boundary Green function over all times and the surface source region gives the fraction that has originated from that source, i.e., $m_k = \sum_{t=0}^{N_t-1} \mathbf{r}_k^T \mathbf{g}(i)$, which is calculated from the northern and southern sources in Table 1. We find that the Pacific core has a 74/23 southern/northern source breakdown, and the Atlantic core site has a 13/81 breakdown, where the percentages do not add to 100% because of the small influence of subtropical and tropical waters. In analogy with these values, we set $m_{A1} = m_{B2} = 0.8$ and $m_{B1} = m_{A2} = 0.2$ and solve for the time-variable history of the surface concentrations (Figure 9). In this case, the internal ocean pathways do not vary in time and there is no lag due to tracer transit, but a 4,000 year lag appears in the idealized sediment core records.

[30] This idealized data can only be explained in the case that the two core sites have differing source water compositions, as the set of equations would not have been invertible if $m_{A1} = m_{B1}$ and $m_{A2} = m_{B2}$. With the differing compositions, a lag in surface changes is communicated to the two core sites, although the lag is somewhat diminished. In this case, the deep ocean does not convey much water sequentially from the Atlantic core to the Pacific core without alteration by mixing with new water masses. This breakdown of the one-dimensional conveyor permits the 4,000 year lag to be explained by regionally varying surface changes.

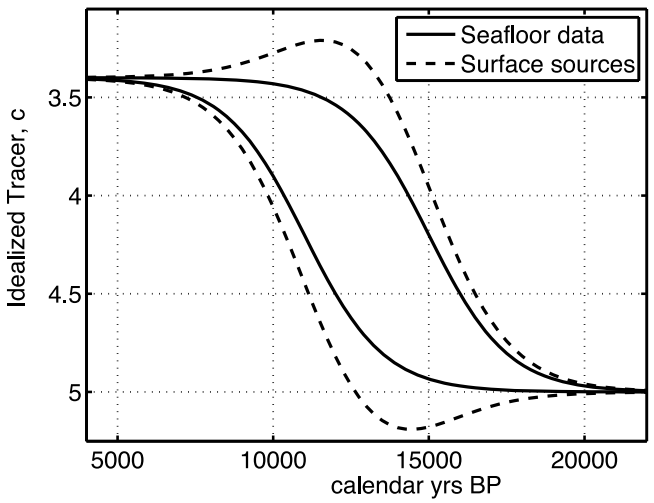

Figure 9. Idealized case with synthetic observations of a tracer (solid) that records a 4,000 year lag in the midpoint of the Last Termination and surface values (dashed) of two sources that explain the observations. This example uses the following parameters: $a = 0.8$, $T_D = 8000$, and $c_{mid} = 4.2$.

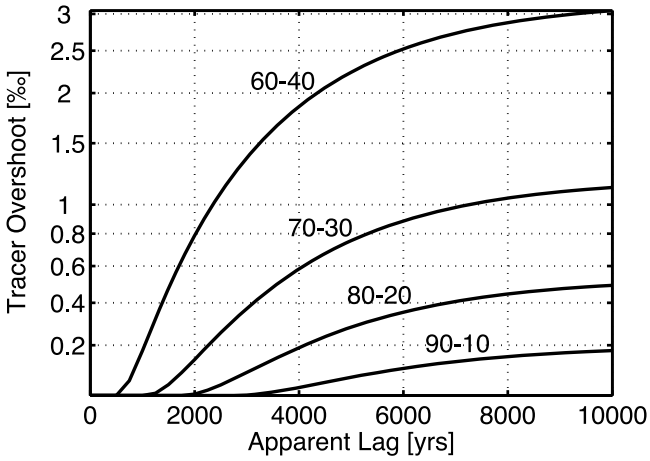

Figure 10. Idealized tracer overshoot necessary to explain a particular deep-sea lag in synthetic observations, given a 2 water mass decomposition (labeled in terms of percentage of waters from two sources). Note the logarithmic scale on the y axis.

[31] When the lag in the idealized observations is increased from 4,000 to 8,000 years, a solution can still be found and there is no limit to the length of the apparent lag that can result from the mixing of two surface sources so long as the surface conditions are freely variable. For any lag, the transition occurs in three distinct phases: (1) destructive interference of source changes at one core site, (2) constructive interference at both core sites, and (3) destructive interference at the other site. The idealized case is symmetric with respect to the two cores, and thus phase 1 is a mirror image of phase 3. Destructive interference refers to compensating changes from the two surface sources resulting in no signal being recorded at the core site. The destructive interference phases are associated with overshoots in the surface tracer values outside of the initial and final tracer values (i.e, a wider range of the surface tracer conditions), where the size of the overshoot must be larger for longer lags. To explain a 4,000 year lag, the overshoot is a relatively small 1/8 of the total transition signal.

[32] The required overshoots depend upon both the apparent lag and the water mass composition (Figure 10). If the two core sites have a more similar composition, the necessary overshoot increases, and for the case where the composition is a 50–50 mix, there is no solution. For an 80–20 mix of sources, the observed 4,000 year lag requires a 0.2‰ overshoot, but the overshoot rises to 0.6‰ for a 70–30 mix. With independent estimates of the water mass distribution, this signal should be detectable in marine sediments were it occurring.

[33] Is it possible for southern and northern source $\delta^{18}O_w$ values to have opposing trends in time? In the case where the $\delta^{18}O$ signal of the LGM is not globally synchronous, southern source values effectively continue their pre-LGM trend toward higher $\delta^{18}O$ even while the northern source waters are being warmed or diluted by low $\delta^{18}O$ ice melt. Destructive interference is a natural consequence of the LGM isotopic signal being initiated in the Northern Hemisphere and only starting later around Antarctica. At the Pacific core site, the North Atlantic surface signal of the Termination is effectively canceled by the still rising Antarctic $\delta^{18}O_w$ signal in this scenario, giving no signal of the Termination until 15 kyr BP.

6.2. Globally Uniform Surface Scenario

[34] We have shown that a deep interbasin lag may be created by lags in surface boundary conditions and tracer transport interference, but the simple example did not require a delay due to transport rates. To isolate the effect of circulation rates, we repeat the calculations of section 5 with the restriction that surface boundary conditions vary in a globally uniform way. In this case, the solution has the form: $\mathbf{x} = \mathbf{x}_0 + \Gamma\mathbf{u}$, where $\mathbf{u}$ is a vector composed of globally uniform surface shifts at all times from 40 kyr BP to present, and Γ is a matrix that maps each value of $\mathbf{u}$ onto the entire surface at the proper time, t. The solution method of this more restrictive problem is detailed in Appendix C.

[35] The best solution of the globally uniform case is a scenario where the core data can be fit before the Last Glacial Maximum and during the Holocene, but neither the Atlantic nor the Pacific core data can be fit within their uncertainty during the Last Termination (Figure 11). The normalized value of J_{data} (i.e., J_{data}/N_{obs}) is 11.4, corresponding to a standard error of 0.27‰. Instead of capturing the 4,000 year lag, this estimate is somewhere between the Atlantic and Pacific data and is not an acceptable solution to the problem. Defining the lag to be the timescale that maximizes the cross-correlation between two time series [*Delhez and Deleersnijder*, 2008], the Atlantic site leads the Pacific by 875 years in this case.

[36] The response of the ocean to globally uniform surface changes can be derived from the full tracer transport model (Appendix D). There are just two master global response functions (or TTDs) in the model: one for each of the core sites (Figure 12). These TTDs are right-skewed distributions, although the tail is thinner than the canonical inverse Gaussian distribution [e.g., *Peacock and Maltrud*, 2006]. Each TTD is a distribution with a multitude of timescales,

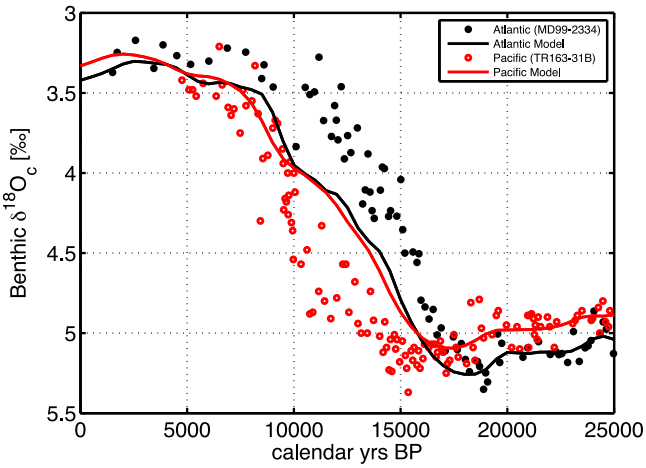

Figure 11. A best fit to the paleo-data with the tracer transport model restricted to have globally uniform surface changes. Neither the Atlantic nor Pacific data can be fit within their uncertainty.

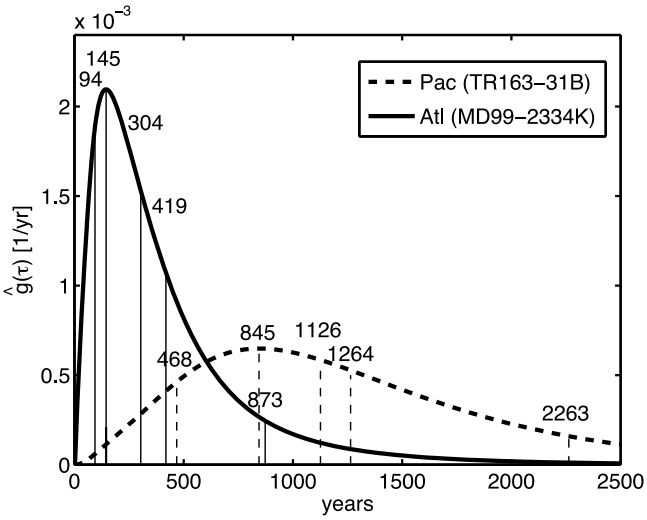

Figure 12. Impulse response to a globally uniform sea surface change of a passive tracer (i.e., TTD or age spectra) at core sites TR163-31B in the eastern Pacific (dashed) and MD99-2334K in the North Atlantic (solid). For each distribution, multiple timescales are marked by vertical lines: (from left to right) 10% signal arrival time, mode of the distribution, median age, mean age, and 90% equilibrium time.

including the 10% signaling time, the mean age, the median age, and the 90% equilibrium time, where the timescales vary from as short as 94 years to as long as 2,263 years.

[37] Of the myriad timescales, which ones matter for interpreting the lag between two time series? The median age defines the time for 50% of a signal to arrive, and thus, the observed lag in the arrival of the midpoint of the Termination is equal to the difference between the median ages of the two distributions (1, 126 − 304 = 822 years). The Atlantic-Pacific lag in the restricted inversion is consistent with this explanation, where the sea surface leads the Pacific by 1,175 years and the Atlantic by 375 years and thus the lag is expected to be 800 years [see also *Delhez and Deleersnijder*, 2008]. The largest possible lags produced by the ocean response to a globally uniform surface change are therefore limited to be no larger than the median age of the ocean, much shorter than the 4,000 year lag and explaining why the inversion of this section could not fit the data.

6.3. Comparison to Previous Studies

[38] *Duplessy et al.* [1991] suggested that the deep radiocarbon age provides information about the expected lag. The radiocarbon age is systematically biased to be younger than the mean age [*Waugh et al.*, 2003] and GLODAP radiocarbon data constrain the bias to be on the order of 100 years [*Gebbie and Huybers*, 2012]. The median age is also younger than the mean age, and fortuitously the radiocarbon age is similar to the median age. Thus, the interbasin radiocarbon age difference is a good approximation to the lag that would be expected by surface-to-deep transit times, although this is subject to the stringent assumption that the surface tracer change is globally uniform. Furthermore, there is nothing fundamental that requires the radiocarbon age to always be a good indicator. In any case, these lags due to tracer transit are considerably smaller than the lags that are possible with regional surface changes.

[39] The 90% equilibrium time was defined by *Wunsch and Heimbach* [2008] to represent the time it takes for the ocean to equilibrate (within 10%) in response to a global surface concentration change. Using the ECCO/MITgcm state estimate [*Wunsch and Heimbach*, 2007; *Wunsch et al.*, 2009], they calculated a 90% equilibrium time of 2,700 years near the Pacific core site and 600 years near the Atlantic core site (although shallower at 1950 m depth), and their major point, that long timescales exist in the ocean, agrees with the results from our empirically derived ocean circulation. If the Last Termination were well approximated by a globally uniform change, however, the observed 4,000 year lag would occur when 50% of the glacial-interglacial signal arrives, and thus, the median age is more appropriate and significantly shorter than the 90% equilibrium time. *Wunsch and Heimbach* [2008] suggest that long timescales are also possible with regional tracer injections, later confirmed by *Siberlin and Wunsch* [2011] and this study.

6.4. Uncertainty Analysis

[40] A least squares error analysis indicates that the source values are estimated to better than 0.2‰, but these errors are calculated under the assumption that the circulation pathways are unchanging. Here we explore the sensitivity of the results to a changed water mass decomposition, following a conventional paleoceanographic interpretation that the northern source waters had shoaled during the LGM [*Curry and Oppo*, 2005; *Marchitto and Broecker*, 2006], although we wish to emphasize that the competing influence of changed surface boundary conditions has still not been ruled out [e.g., *Rutberg and Peacock*, 2006; *Burke et al.*, 2011]. To approximate the LGM effect, we move the modern-day water mass decomposition of *Gebbie and Huybers* [2010] upward by 1000 meters, finding that the Atlantic core site has 20% more southern source waters, and that the Pacific core site is essentially unchanged due to the homogeneity of the deep ocean there. In the LGM-like water mass decomposition, the estimated Antarctic and North Atlantic end-members for $\delta^{18}O_w$ are changed by 0.1‰ and 0.3‰ at 19 kyr BP, respectively. The estimated end-members are very sensitive during the Termination, such as at 15 kyr BP, where changes are 0.5‰ and 0.8‰. Of course, the LGM-like water mass decomposition may be inappropriate at 15 kyr BP, leading to an overestimate of the potential uncertainty.

[41] Our results rely upon a small subset of the total number of paleoceanographic records available and changes in the water mass decomposition may be proven if additional data constraints are provided to the problem [e.g., *Waelbroeck et al.*, 2011]. If our results hold as more data are included, the changes in the $\delta^{18}O$ end-member may reflect dilution of the sea surface by low $\delta^{18}O$ waters from ice sheet melt. Here, we only model the portion of the $\delta^{18}O$ cycle that is internal to the ocean, and another step must be taken to relate the ocean surface changes to changes in the cryosphere.

[42] All of the calculations of this work use Dirichlet boundary conditions where surface concentration is prescribed [e.g., *Rutberg and Peacock*, 2006]. There is always a set of Neumann boundary conditions that correspond to the

Dirichlet boundary conditions, so either formulation can be used in the inverse problem. In contrast to the work of *Primeau and Deleersnijder* [2009] who isolate the effect of meltwater injection through flux boundary conditions, however, the reconstructed surface concentrations of this work cannot differentiate between the effects of evaporation, precipitation, and runoff.

7. Conclusion

[43] A well-dated pair of benthic $\delta^{18}O_c$ records indicates that the signal of the midpoint of the Last Termination arrived 4,000 years earlier in the deep Atlantic than the Pacific, and we find a scenario where such a long lag could occur through a series of regional changes in $\delta^{18}O_w$ and temperature. In order to accurately simulate the fate of tracer sources at many surface locations, we use an ocean circulation model empirically determined by the TMI method and we develop a boundary Green function inverse technique in order to fit the paleo-data over 35,000 years. The circulation model resolves 2,806 individual surface locations that can all serve as sources of tracer, and the model captures the advective-diffusive nature of the modern circulation in an accurate way as it is trained with over a million tracer observations. If the ocean circulation is assumed to be steady, there is no globally uniform tracer change that can explain the 4,000 year lag, but there is a regionally varying pattern that can fit benthic $\delta^{18}O_c$, Mg/Ca-derived temperature information, and pore water data. The reconstructed changes in surface $\delta^{18}O_w$ are consistent with the late timing of the local LGM around Antarctica and suggest ice sheet melt was being led by the northern hemisphere during the Last Termination.

[44] Previously it was thought that the lag due to tracer transport could not be much longer than the radiocarbon age of the ocean, approximately 1,500 years in the deep Pacific [e.g., *Broecker et al.*, 1988; *Duplessy et al.*, 1991]. For a globally uniform surface tracer change, this is true, as the lag is limited to be near the median age difference of two sites, and the median age is usually similar to the radiocarbon age. More generally, lags of any duration can appear between two time series in the deep ocean when regional patterns of surface tracer injection occur and the two sites are bathed in sufficiently different mixtures of source water. Thus, the 4,000 year lag in the paleo-data can be explained by a lag in surface conditions and destructive and constructive interference between northern and southern source waters at the two core sites. For such a long lag, an overshoot in source property values is expected, and is a natural consequence of the asynchronous isotopic signal of the LGM at the sea surface.

[45] This work does not imply that the circulation pathways of the ocean were unchanged between the modern-day and the LGM, but rather that the interpretation of the Atlantic-Pacific lag in these two sediment core records does not require such a change. While there seems to be good evidence from other paleo-data that pathways did change, tracer inversions have not yet concluded that this must be so [e.g., *LeGrand and Wunsch*, 1995; *Gebbie and Huybers*, 2006; *Huybers et al.*, 2007; *Marchal and Curry*, 2008; *Burke et al.*, 2011]. By adding tracer constraints with increased temporal and spatial resolution, there is promise that the framework of this study can be used to detect such circulation changes in future work.

Appendix A: Calculation of Boundary Green functions

[46] Introducing the vector $\mathbf{c}$ to be the global distribution of any conservative tracer in vector form, a global advection–diffusion balance can be written:

$$\frac{\partial \mathbf{c}}{\partial t} = \mathcal{L}\mathbf{c}, \tag{A1}$$

where the matrix $\mathcal{L}$ is the tracer transport operator. Using a stiff, variable-order solver based on numerical differentiation formulas, we step the tracer forward in time, symbolically written

$$\mathbf{c}(t+\Delta t) = \mathbf{L}\mathbf{c}(t) + \mathbf{B}\mathbf{c}_b(t+\Delta t) \tag{A2}$$

where $\mathbf{L}$ is the discrete-time equivalent of $\mathcal{L}$, and $\mathbf{B}$ is a matrix that maps from the surface boundary to the global model grid in order to enforce Dirichlet (concentration) boundary conditions of $\mathbf{c}_b$. With 4° by 4° horizontal resolution and 33 vertical levels, the matrix $\mathbf{L}$ is highly sparse with a size of 74,064 by 74,064.

[47] By performing multiple time steps and rearranging the time indices, a simplified relationship for the tracer distributions at time t is found:

$$\mathbf{c}(t) = \mathbf{L}^N\mathbf{c}(t-N\Delta t) + \sum_{i=0}^{N-1}\mathbf{L}^i\ \mathbf{B}\ \mathbf{c}_b(t-i\Delta t). \tag{A3}$$

If N is large enough, the memory of the past conditions is ultimately lost, and the first term in equation (A3) is eliminated. Focusing on a point and introducing the vector $\mathbf{r}$ to be a mapping onto that point, we obtain

$$c(r,t) = \sum_{i=0}^{N-1}\mathbf{r}^T\ \mathbf{L}^i\ \mathbf{B}\ \ \mathbf{c}_b(t-i\Delta t) \tag{A4}$$

where we use the 8 closest grid points weighted by their distance away from the core site to form $\mathbf{r}$. Defining $\mathbf{g}(i)^T = \mathbf{r}^T\mathbf{L}^i\mathbf{B}$, this equation is simplified into the boundary Green function form of the transport model

$$c(r,t) = \sum_{i=0}^{N-1}\mathbf{g}(i)^T\ \ \mathbf{c}_b(t-i\Delta t), \tag{A5}$$

where the tracer concentration at an interior point is a linear function of the surface concentration at previous times. Only the lag, $i\Delta t$, is important for determining the relevant function $\mathbf{g}(i)$. To calculate $\mathbf{g}(i)$, we transpose the definition of the boundary Green function to obtain: $\mathbf{g}(i) = \mathbf{B}^T\mathbf{L}^{Ti}\mathbf{r}$, where $\mathbf{L}^T$ is the adjoint model, and $\mathbf{L}^{Ti}$ indicates i timesteps of the adjoint. The adjoint tracer transport equation runs backwards in time with an initial condition of $\mathbf{r}$ (a source at the seafloor core sites) and reversed advection.

Appendix B: Solution Method for Temporally and Spatially Varying Changes

[48] When considering all possible regional and local changes, equation (4) has 451,766 unknowns and 284 observational constraints, indicating a highly underdetermined

problem. It is not practical to invert the sum, $\mathbf{S}_{xy}^{-1} + \mathbf{S}_t^{-1}$, because it has the dimension of the state squared (451, 766 × 451, 766) and is nondiagonal. By keeping the spatial and temporal covariance matrices separate, we exploit the special structure of $\mathbf{S}_{xy}^{-1}$ that would otherwise vanish when $\mathbf{S}_{xy}^{-1}$ is added to $\mathbf{S}_t^{-1}$. Therefore, we append the temporal constraints to the observational constraints:

$$\mathbf{E} = \begin{pmatrix} \mathbf{G} \\ \mathbf{F} \end{pmatrix}, \ \mathbf{h} = \begin{pmatrix} \mathbf{y} \\ 0 \end{pmatrix}, \ \mathbf{R}^{-1} = \begin{pmatrix} \mathbf{W}^{-1} & 0 \\ 0 & \mathbf{W}_t^{-1} \end{pmatrix}, \tag{B1}$$

where $\mathbf{F}$ was defined in equation (5) to calculate the difference between water mass values over the 14 sub-regions and $\mathbf{W}_t$ was also defined in that section. Now the cost function becomes

$$\mathrm{J} = (\mathbf{E}\mathbf{u} - \mathbf{h})^T \mathbf{R}^{-1} (\mathbf{E}\mathbf{u} - \mathbf{h}) + \mathbf{u}^T \mathbf{S}_{xy}^{-1} \mathbf{u}, \tag{B2}$$

which has the solution:

$$\mathbf{u} = \mathbf{S}_{xy} \mathbf{E}^T \left(\mathbf{E} \mathbf{S}_{xy} \mathbf{E}^T + \mathbf{R} \right)^{-1} \mathbf{h}, \tag{B3}$$

and $\mathbf{x} = \mathbf{x}_0 + \mathbf{u}$. Recognizing that the matrix $\mathbf{S}_{xy}^{-1}$ is block diagonal and composed of N_t blocks of size 2,806 by 2,806, we invert the matrix by determining the inverse of each block independently with a Cholesky decomposition method. $\mathbf{R}^{-1}$ is also easily inverted because it is a diagonal matrix. Now the solution relies upon the inverse of a 2, 524 dimension square matrix (284 observational constraints plus 2,240 temporal smoothness constraints) – which is larger than the globally uniform surface case but still computationally tractable.

Appendix C: Solution Method for Globally Uniform Changes

[49] To solve the inverse problem in the restricted case where all surface changes are globally uniform, we make a variable transformation to take the specified solution form, $\mathbf{x} = \mathbf{x}_0 + \Gamma \mathbf{u}$, into account:

$$\hat{\mathbf{G}} = \mathbf{G}\Gamma, \ \hat{\mathbf{S}}_{xy}^{-1} = \Gamma^T \mathbf{S}_{xy}^{-1} \Gamma, \ \hat{\mathbf{S}}_t^{-1} = \Gamma^T \mathbf{S}_t^{-1} \Gamma. \tag{C1}$$

Then the cost function (equation (6)) is simplified:

$$\hat{\mathrm{J}} = \left(\hat{\mathbf{G}}\mathbf{u} - \mathbf{y} \right)^T \mathbf{W}^{-1} \left(\hat{\mathbf{G}}\mathbf{u} - \mathbf{y} \right) + \mathbf{u}^T \left(\hat{\mathbf{S}}_{xy}^{-1} + \hat{\mathbf{S}}_t^{-1} \right) \mathbf{u}. \tag{C2}$$

There are $N_t = 161$ elements of the $\mathbf{u}$ vector subject to the $N_{obs} = 284$ observations, leading to a formally overdetermined problem with solution [e.g., *Wunsch*, 1996]

$$\mathbf{u} = \left(\hat{\mathbf{G}}^T \mathbf{W}^{-1} \hat{\mathbf{G}} + \hat{\mathbf{S}}_{xy}^{-1} + \hat{\mathbf{S}}_t^{-1} \right)^{-1} \hat{\mathbf{G}}^T \mathbf{W}^{-1} \mathbf{y} \tag{C3}$$

that relies upon the inversion of a matrix of size $N_t \times N_t$, which is practical. After solving for $\mathbf{u}$, the solution $\mathbf{x}$ is estimated by back substitution into the specified form of the solution.

Appendix D: Global Response Functions

[50] The global-response model is $\hat{\mathbf{G}}\mathbf{u} = \mathbf{y}$, where $\hat{\mathbf{G}}$ includes the relevant transport dynamics, $\mathbf{u}$ is a global surface concentration perturbation, and $\mathbf{y}$ is the deep ocean response. The transport dynamics are determined by $\hat{\mathbf{G}} = \mathbf{G}\Gamma$, where each row of $\hat{\mathbf{G}}$ is the sum of $\mathbf{g}(i)$ over the entire surface, which is interpretable as the fraction of tracer that originates from the surface with a lag or transit time of $i\Delta t$. Therefore $\hat{\mathbf{G}}$ is a matrix with transit time distributions making up each row, all referenced to the appropriate observational time and core site.

[51] **Acknowledgments.** We thank Francois Primeau, Luke Skinner, an anonymous associate editor, and the Editor, Chris Charles, for thorough and constructive reviews. We also thank Dan Amrhein and Kuo-Fang (Denner) Huang for helpful calculations, Ken Decoteau for technical assistance, and Holly Dail, Peter Huybers, Olivier Marchal, and Carl Wunsch for comments. G.G. is supported by NSF grant OIA-1124880 and the WHOI Arctic Research Initiative.

References

Adkins, J., K. McIntyre, and D. Schrag (2002), The salinity, temperature, and $\delta^{18}O$ of the glacial deep ocean, *Science*, *298*, 1724–1725.

Bennett, A. F. (1992), *Inverse Methods in Physical Oceanography*, 346 pp., Cambridge Univ. Press, Cambridge, U. K.

Boyle, E., and L. Keigwin (1982), Deep circulation of the North Atlantic over the last 200,000 years: Geochemical evidence, *Science*, *218*(4574), 784–787.

Broecker, W. S., and T. H. Peng (1982), *Tracers in the Sea*, Lamont-Doherty Earth Obs., Columbia Univ., Palisades, N. Y.

Broecker, W. S., and J. van Donk (1970), Insolation changes, ice volumes, and the O^{18} record in deep-sea cores, *Rev. Geophys.*, *8*(1), 169–198.

Broecker, W. S., D. Oppo, T. Peng, W. Curry, M. Andree, W. Wolfli, and G. Bonani (1988), Radiocarbon-based chronology for the $^{18}O/^{16}O$ record for the Last Deglaciation, *Paleoceanography*, *3*(4), 509–515.

Burke, A., O. Marchal, L. Bradtmiller, J. McManus, and R. François (2011), Application of an inverse method to interpret $^{231}Pa/^{230}Th$ observations from marine sediments, *Paleoceanography*, *26*, PA1212, doi:10.1029/2010PA002022.

Clark, P., A. Dyke, J. Shakun, A. Carlson, J. Clark, B. Wohlfarth, J. Mitrovica, S. Hostetler, and A. McCabe (2009), The last glacial maximum, *Science*, *325*(5941), 710–714.

Condron, A., and P. Winsor (2011), A subtropical fate awaited freshwater discharged from glacial Lake Aggasiz, *Geophys. Res. Lett.*, *38*, L03705, doi:10.1029/2010GL046011.

Curry, W., and D. Oppo (2005), Glacial water mass geometry and the distribution of $\delta^{13}C$ of ΣCO_2 in the western Atlantic Ocean, *Paleoceanography*, *20*, PA1017, doi:10.1029/2004PA001021.

Deleersnijder, E., J. M. Campin, and E. J. M. Delhez (2001), The concept of age in marine modelling I. Theory and preliminary model results, *J. Mar. Syst.*, *28*(3–4), 229–267.

Delhez, É. J. M., and É. Deleersnijder (2008), Age and the time lag method, *Cont. Shelf Res.*, *28*(8), 1057–1067.

Delhez, É. J. M., J. Campin, A. Hirst, and É. Deleersnijder (1999), Toward a general theory of the age in ocean modelling, *Ocean Modell.*, *1*(1), 17–27.

Delhez, É. J. M., É. Deleersnijder, A. Mouchet, and J. M. Beckers (2003), A note on the age of radioactive tracers, *J. Mar. Syst.*, *38*(3–4), 277–286.

Duplessy, J., E. Bard, M. Arnold, N. Shackleton, J. Duprat, and L. Labeyrie (1991), How fast did the ocean–atmosphere system run during the last deglaciation?, *Earth Planet. Sci. Lett.*, *103*(1–4), 27–40.

England, M. H. (1995), The age of water and ventilation timescales in a global ocean model, *J. Phys. Oceanogr.*, *25*(11), 2756–2777.

Erez, J., and B. Luz (1983), Experimental paleotemperature equation for planktonic foraminifera, *Geochim. Cosmochim. Acta*, *47*(6), 1025–1031.

Fairbanks, R., et al. (2005), Radiocarbon calibration curve spanning 0 to 50,000 years BP based on paired $^{230}Th/^{234}U/^{238}U$ and ^{14}C dates on pristine corals, *Quat. Sci. Rev.*, *24*(16–17), 1781–1796.

Fofonoff, N. P., and R. C. Millard Jr. (1983), Algorithms for computation of fundamental properties of seawater, *UNESCO Tech. Pap. Mar. Sci. 44*, 58 pp., UNESCO, Paris.

Gebbie, G., and P. Huybers (2006), Meridional circulation during the Last Glacial Maximum explored through a combination of δ^{18}O observations and a geostrophic inverse model, *Geochem. Geophys. Geosyst.*, *7*, Q11N07, doi:10.1029/2006GC001383.

Gebbie, G., and P. Huybers (2010), Total matrix intercomparison: a method for resolving the geometry of water-mass pathways, *J. Phys. Oceanogr.*, *40*(8), 1710–1728, doi:10.1175/2010JPO4272.1.

Gebbie, G., and P. Huybers (2011), How is the ocean filled?, *Geophys. Res. Lett.*, *38*, L06604, doi:10.1029/2011GL046769.

Gebbie, G., and P. Huybers (2012), The mean age of ocean waters inferred from radiocarbon observations: sensitivity to surface sources and accounting for mixing histories, *J. Phys. Oceanogr.*, *42*(2), 291–305, doi:10.1175/JPO-D-11-043.1.

Gebbie, G., P. Heimbach, and C. Wunsch (2006), Strategies for Nested and Eddy-Permitting State Estimation, *J. Geophys. Res.*, *111*, C10073, doi:10.1029/2005JC003094.

Gouretski, V., and K. Koltermann (2004), WOCE Global Hydrographic Climatology, *Tech. Rep. 35*, Bundesamtes fur Seeschifffahrt und Hydrogr., Hamburg, Germany.

Haine, T. W. N., and T. M. Hall (2002), A generalized transport theory: Water-mass composition and age, *J. Phys. Oceanogr.*, *32*(6), 1932–1946.

Hall, T., and T. Haine (2002), On ocean transport diagnostics: The idealized age tracer and the age spectrum, *J. Phys. Oceanogr.*, *32*, 1987–1991.

Hartzell, S. (1978), Earthquake aftershocks as Green's functions, *Geophys. Res. Lett.*, *5*(1), 1–4.

Hughen, K., S. Lehman, J. Southon, J. Overpeck, O. Marchal, C. Herring, and J. Turnbull (2004), ^{14}C activity and global carbon cycle changes over the past 50,000 years, *Science*, *303*(5655), 202–207.

Huybers, P., G. Gebbie, and O. Marchal (2007), Can paleoceanographic tracers constrain meridional circulation rates?, *J. Phys. Oceanogr.*, *37*(2), 394–407, doi:10.1175/JPO3018.1.

Keigwin, L., G. Jones, and P. Froelich (1992), A 15,000 year paleoenvironmental record from Meiji Seamount, far northwestern Pacific, *Earth Planet. Sci. Lett.*, *111*(2), 425–440.

Key, R. M., A. Kozyr, C. L. Sabine, K. Lee, R. Wanninkhof, J. L. Bullister, R. A. Feely, F. J. Millero, C. Mordy, and T.-H. Peng (2004), A global ocean carbon climatology Results from Global Data Analysis Project (GLODAP), *Global Biogeochem. Cycles*, *18*, GB4031, doi:10.1029/2004GB002247.

Khatiwala, S., M. Visbeck, and P. Schlosser (2001), Age tracers in an ocean GCM, *Deep Sea Res., Part I*, *48*(6), 1423–1441.

LeGrand, P. and C. Wunsch (1995), Constraints from paleotracer data on the North Atlantic circulation during the Last Glacial Maximum, *Paleoceanography*, *10*(6), 1011–1045, doi:10.1029/95PA01455.

LeGrande, A. N., and G. A. Schmidt (2006), Global gridded data set of the oxygen isotopic composition in seawater, *Geophys. Res. Lett.*, *33*, L12604, doi:10.1029/2006GL026011.

Marchal, O., and W. Curry (2008), On the abyssal circulation in the glacial Atlantic, *J. Phys. Oceanogr.*, *38*(9), 2014–2037.

Marchitto, T., and W. Broecker (2006), Deep water mass geometry in the glacial Atlantic Ocean: A review of constraints from the paleonutrient proxy Cd/Ca, *Geochem. Geophys. Geosyst.*, *7*, Q12003, doi:10.1029/2006GC001323.

Martin, P., D. Lea, Y. Rosenthal, N. Shackleton, M. Sarnthein, and T. Papenfuss (2002), Quaternary deep sea temperature histories derived from benthic foraminiferal Mg/Ca, *Earth Planet. Sci. Lett.*, *198*(1–2), 193–209.

Matsumoto, K. (2007), Radiocarbon-based circulation age of the world oceans, *J. Geophys. Res.*, *112*, C09004, doi:10.1029/2007JC004095.

Mix, A., and W. Ruddiman (1984), Oxygen-isotope analyses and Pleistocene ice volumes, *Quat. Res.*, *21*(1), 1–20.

Morse, P. M., and H. Feshbach (1953), *Methods of Theoretical Physics*, McGraw-Hill, New York.

O'Neil, J., R. Clayton, and T. Mayeda (1969), Oxygen isotope fractionation in divalent metal carbonates, *J. Chem. Phys.*, *51*, 5547.

Peacock, S., and M. Maltrud (2006), Transit-time distributions in a global ocean model, *J. Phys. Oceanogr.*, *36*(3), 474–495.

Primeau, F. (2005), Characterizing transport between the surface mixed layer and the ocean interior with a forward and adjoint global ocean transport model, *J. Phys. Oceanogr.*, *35*(4), 545–564.

Primeau, F., and E. Deleersnijder (2009), On the time to tracer equilibrium in the global ocean, *Ocean Sci*, *5*, 13–28.

Primeau, F. W., and M. Holzer (2006), The ocean's memory of the atmosphere: Residence-time and ventilation-rate distributions of water masses, *J. Phys. Oceanogr.*, *36*(7), 1439–1456.

Rutberg, R., and S. Peacock (2006), High-latitude forcing of interior ocean δ^{13}C, *Paleoceanography*, *21*, PA2012, doi:10.1029/2005PA001226.

Shackleton, N. (1974), Attainment of isotopic equilibrium between ocean water and the benthonic foraminifera genus Uvigerina: Isotopic changes in the ocean during the last glacial, *Colloq. Int. C. N. R. S.*, *219*, 203–209.

Shackleton, N., J. Duplessy, M. Arnold, P. Maurice, M. Hall, and J. Cartlidge (1988), Radiocarbon age of last glacial Pacific deep water, *Nature*, *335*(6192), 708–711.

Shackleton, N., R. Fairbanks, T. Chiu, and F. Parrenin (2004), Absolute calibration of the Greenland time scale: implications for Antarctic time scales and for δ^{14}C, *Quat. Sci. Rev.*, *23*(14–15), 1513–1522.

Siberlin, C., and C. Wunsch (2011), Oceanic tracer and proxy time scales revisited, *Clim. Past*, *7*, 27–39.

Skinner, L. C., and N. J. Shackleton (2004), Rapid transient changes in northeast Atlantic deep water ventilation age across Termination I, *Paleoceanography*, *19*, PA2005, doi:10.1029/2003PA000983.

Skinner, L. C., and N. J. Shackleton (2005), An Atlantic lead over Pacific deep-water change across Termination I: Implications for the application of the marine isotope stage stratigraphy, *Quat. Sci. Rev.*, *24*(5–6), 571–580.

Skinner, L. C., N. J. Shackleton, and H. Elderfield (2003), Millennial-scale variability of deep-water temperature and $\delta^{18}O_{dw}$ indicating deep-water source variations in the Northeast Atlantic, 0–34 cal. ka BP, *Geochem. Geophys. Geosyst.*, *4*(12), 1098, doi:10.1029/2003GC000585.

Skinner, L. C., et al. (2007), Deep-water temperature, stable oxygen isotopes and Mg/Ca on benthic foraminifera of sediment core MD99-2334, http://doi.pangaea.de/10.1594/PANGAEA.619066, PANGAEA, Network for Geol. and Environ. Data, Germany.

Waelbroeck, C., L. Skinner, L. Labeyrie, J.-C. Duplessy, E. Michel, N. V. Riveiros, J.-M. Gherardi, and F. Dewilde (2011), The timing of deglacial circulation changes in the Atlantic, *Paleoceanography*, *26*, PA3213, doi:10.1029/2010PA002007.

Waugh, D. W., T. M. Hall, and T. W. N. Haine (2003), Relationships among tracer ages, *J. Geophys. Res.*, *108*(C5), 3138, doi:10.1029/2002JC001325.

Wunsch, C. (1996), *The Ocean Circulation Inverse Problem*, 437 pp., Cambridge Univ. Press, New York.

Wunsch, C. (2002), Oceanic age and transient tracers: Analytical and numerical solutions, *J. Geophys. Res.*, *107*(C6), 3048, doi:10.1029/2001JC000797.

Wunsch, C., and P. Heimbach (2007), Practical global oceanic state estimation, *Phys. D*, *230*(1–2), 192–208.

Wunsch, C., and P. Heimbach (2008), How long to oceanic tracer and proxy equilibrium?, *Quat. Sci. Rev.*, *27*, 637–651.

Wunsch, C., P. Heimbach, R. Ponte, and I. Fukumori (2009), The global general circulation of the oceans estimated by the ECCO-Consortium, *Oceanography*, *20*(2), 88–103.